

Materials Advances

Accepted Manuscript

This article can be cited before page numbers have been issued, to do this please use: S. Chaudhary, K. P. S. Parmar, P. Jain and A. Vij, *Mater. Adv.*, 2025, DOI: 10.1039/D5MA00414D.



This is an Accepted Manuscript, which has been through the Royal Society of Chemistry peer review process and has been accepted for publication.

Accepted Manuscripts are published online shortly after acceptance, before technical editing, formatting and proof reading. Using this free service, authors can make their results available to the community, in citable form, before we publish the edited article. We will replace this Accepted Manuscript with the edited and formatted Advance Article as soon as it is available.

You can find more information about Accepted Manuscripts in the [Information for Authors](#).

Please note that technical editing may introduce minor changes to the text and/or graphics, which may alter content. The journal's standard [Terms & Conditions](#) and the [Ethical guidelines](#) still apply. In no event shall the Royal Society of Chemistry be held responsible for any errors or omissions in this Accepted Manuscript or any consequences arising from the use of any information it contains.

Photoinduced Supercapacitance and Photocatalytic Performance of TiO₂ Enhanced by Electronic Band Structure Modification Using Cu-doping

Sakshi Chaudhary¹, Kanak Pal Singh Parmar^{1, *}, Prachi Jain², Ankush Vij³

¹Department of Physics, Applied Science Cluster, UPES, Dehradun-248001 Uttarakhand, India

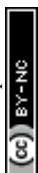
²Materials Analysis and Research Laboratory, Netaji Subhas University of Technology,
Sector-3, Dwarka, New Delhi-110078, India

³Dept of Physics & Astrophysics, Central University of Haryana (CUH) Mahendergarh-12303, Haryana, India

*Corresponding author email: kpsparmar@ddn.upes.ac.in

Abstract

We demonstrate that doping a modest quantity of Cu impurity into anatase TiO_2 significantly enhances its photoinduced electrocatalytic supercapacitance by about 84% and its photocatalytic activity by more than twofold. X-ray diffraction (XRD), Raman spectroscopy, X-ray photoelectron spectroscopy (XPS), and electron paramagnetic resonance (EPR) spectroscopy analyses validate that the Cu dopant is fully incorporated into the tetragonal crystal structure of the host material and creates Ti^{3+} and oxygen vacancies. Furthermore, UV-vis spectroscopy and photoluminescence (PL) studies demonstrate that the smallest optical band gap energy (E_b) of 2.85 eV and minimal recombination of photoinduced charge carrier pairs occur at a 3% Cu doping amount. Transmission electron microscopy (TEM) images reveal that pristine TiO_2 and Cu-doped TiO_2 exhibit nearly identical pebble-like nanoparticle morphologies. This 3% Cu-doped TiO_2 demonstrates more than double photodegradation (95.7%; 150 min) of a toxic Rhodamine B dye molecule and a nearly 84% improved supercapacitance (347 F/g; 0.5 M aq. Na_2SO_4 ; pH=7) than that of a pristine anatase TiO_2 . In suitable testing conditions of other electrolytes, molecular dyes, light intensity, etc., Cu-doped TiO_2 with different particle shapes may demonstrate even greater supercapacitive



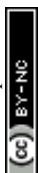
behavior and photodissociation properties, leading to more advantageous applications for photoactive Cu-doped TiO₂ materials.

Keywords: TiO₂, Cu-doping, Optoelectronic, Carriers-separation, Photocatalytic, Photocapacitance

Introduction

Severe contamination of the environment has resulted from the consistent use of traditional energy sources by humans [1]. A major global concern now is the scarcity of sustainable and clean energy sources, which is driving researchers to investigate and create safe, eco-friendly, and energy-efficient alternatives [2–3]. Sunlight is the most abundantly available natural energy resource on Earth; therefore, catalytic reactions on the surface of semiconducting materials, initiated by charge carriers generated under solar light irradiation, offer promising pathways to effectively address the utmost challenges of clean energy generation as well as to mitigate industrial gaseous and water pollutants. Moreover, the demand for energy solutions has significantly increased worldwide, and in this regard, electrochemical supercapacitors have emerged as a promising technology to provide quick power delivery in various applications requiring rapid charging and discharging cycles.

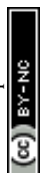
Semiconducting transition metal oxides have been at the forefront of developing innovative solutions for clean energy production and environmental remediation [4-5]. Among the various metal oxides, the inexpensive and nontoxic TiO₂ is recognized for its exceptional resilience in harsh acidic and basic environments. This makes it particularly useful in practically all chemical reactions, and as a result, it has always been a focus of research studies in a variety of practical fields, including photovoltaics, photocatalysis, sensors, charge storage, coatings, and more [6–13]. However, the standalone performance of



TiO₂ as a semiconducting photocatalyst and an electrocatalyst is limited due to its low light absorption, poor photoconductivity, and low ionic diffusivity.

To address these important issues, several strategies have been reported and used to improve the photo- and electro-catalytic performance of TiO₂ material. Some of the often-used strategies include intentionally impurity doping with donors and acceptors, modifying particle size and shape, and creating heterojunctions using appropriate materials [14-17]. It has been shown that doping TiO₂ with metal and non-metal impurities increases its electrical conductivity and decreases its optical bandgap energy. This selective doping technique directly alters the intrinsic unit cell structure and boosts photovoltaic, electrocatalytic, and photocatalytic efficiency, enabling applications of impurity-doped TiO₂ materials in energy and environmental fields [14, 16-20].

Here, we report the simple alcohothermal synthesis of Cu-doped TiO₂ powders and the structural characterization of these powders using X-ray photoelectron spectroscopy (XPS), Raman spectroscopy, UV-vis spectroscopy, photoluminescence (PL) spectroscopy, transmission electron microscopy (TEM), and powder X-ray diffraction (XRD). After determining the optimal concentration of Cu (3%) dopant that produces enhanced light absorption and charge carrier pair dynamics, we evaluate the photoinduced catalytic and electrocatalytic performance of this Cu-doped anatase TiO₂ material under a UV-vis light exposure of a 250 W Hg-lamp (200–450 nm). This entails using galvanostatic charging discharging (GCD) and cyclic voltammetry (CV) tests to monitor the photodegradation of Rhodamine B dye (RhB), an industrial toxic and carcinogenic water pollutant, as well as to assess the capacitive performance and chemical durability of its fabricated electrodes in a neutral (pH=7) 0.5 M Na₂SO₄ aqueous electrolyte solution. Interestingly, this Cu-doped TiO₂ exhibits more than twice the photocatalytic degradation of RhB dye molecules and about



84% higher supercapacitance under UV-vis light (250 W, Hg-lamp, 200–450 nm) conditions than pristine anatase TiO₂.

Experimental Section

Synthesis and Characterization: Powder samples are synthesized as follows: Under constant magnetic stirring (300 rpm), a mixture is made by mixing 2 ml of acetylacetone (Merck, 99.5%) into 30 ml of 2-methoxypropanol (Thermo-Fisher, 99.5%) inside a cylindrical-sized (50 ml) Teflon vessel linked to a stainless-steel autoclave system. Then, 7 millimoles (ca. 2.48 ml) of titanium butoxide (Sigma Aldrich, 99.5%) were directly injected into the mixture, resulting in a yellowish-orange color. After 30 min., 2 ml of triple-deionized water (Millipore, 18.2 MΩ-cm) was added dropwise. The string was stopped after 30 minutes. The tightly sealed system was heated in a hot-air oven (180°C, 12 hr.). The naturally cooled precipitates were filtered and washed with ethanol 2-3 times and then dried in a microwave oven (150°C, 2 hr.). The final powder sample was obtained by hand-grinding using a mortar and pestle. To prepare Cu-doped TiO₂, an appropriate amount of copper (II) acetate monohydrate (Thermo-Fisher, 99.5%) was added to the mixture before adding the titanium butoxide. The subsequent steps in the synthesis process remain the same.

The inherent structural features and optoelectronic characteristics of the samples were mapped out using various experimental techniques. Powder X-ray diffraction (XRD) patterns were recorded at ambient room temperature conditions using a Panalytical X'Pert-Pro diffractometer (operating conditions: Ni-filtered Cu-Kα₁, λ=1.540598 Å, 40 kV, 30 mA, 0.02 deg./sec). Raman (excitation DPSS laser, λ=532 nm, spectral resolution ~1 cm⁻¹) and photoluminescence (PL; excitation LED laser, λ=280 nm, spectral resolution ~1 nm) measurements were carried out at ambient room temperature using a RIM-U-DC Raman spectrophotometer (RI Instruments & Innovation India). Using BaSO₄ as a calibrating



reference, the optical spectra were recorded at ambient room temperature in the range of 300 to 800 nm using a UV-visible (UV-vis) spectrophotometer (WinUV-5000, Agilent Technology) equipped with integrating spheres. The chemical composition and electronic structures were investigated using inductively coupled plasma mass spectroscopy (ICP-MS; Agilent USA; 7900 with UHMI), high-resolution (47 meV) X-ray photoelectron spectroscopy (XPS; Thermo-Fisher Scientific; Al-K α anode source; 1486.6 eV), and electron paramagnetic resonance (EPR) spectroscopy (Bruker; A300-9.5/12/S/W; spectrometer). The XPS samples were prepared as pellets, and the XPS data were then acquired under vacuum conditions with a base pressure of 10^{-7} torr. The binding energies of ionic species were calibrated to the C (1s) peak (284.6 eV) of adventitious surface carbon. The EPR spectra were obtained at room temperature. For EPR measurements, an X-band frequency of 9.843 GHz with a magnetic field sweep range from 0 to 5000 Gauss was used. The structure and morphological features of the powder samples were examined using a TALOS F200 X transmission electron microscope (TEM; Thermo-Fisher) operated at 200 kV, with a point-to-point resolution of 0.16 nm. TEM, and high-resolution TEM (HR-TEM) images were recorded on a carbon-coated copper grid.

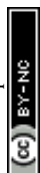
Photocatalytic and Electrochemical (EC) Measurements: The photocatalytic activity of the powder was estimated through the degraded amount of Rhodamine B dye (RhB; Thermo-Fisher, violet color). A standard 50 ml solution of 25 ppm concentration is prepared by dissolving RhB into a mixture (1:1 molar ratio) of ethanol (Thermo-Fisher, 99.5%) and acetonitrile (Sigma Aldrich, 99.5%). A powder sample (5 mg) was then added to this standard solution, and the dispersion was stirred in the dark for 30 min. This dispersion was maintained at a fixed distance (20 cm) from the light source and then irradiated from the top with UV-vis radiation (Techinstro vision, Hg-lamp, 250 W, 200–450 nm) under mild stirring. For every 30-minute duration, ca. 5 mL of the collected liquid dispersion was centrifuged



(5000 rpm, 5 min.), and the remaining dye amount in the liquid supernatant (3 mL) was estimated using a Shimadzu UV-vis spectrophotometer (UV-2600I). The photodegradation performance (C_{RB}) of the powder sample was calculated using the expression $(C_0 - C_t)/C_0$, where C_0 and C_t represent the dye concentration at the starting and at a particular time t , respectively [20].

The electrode of the powder sample is fabricated as follows: 7 mg of powder, 1 mg of double-walled carbon nanotube (SRL, extra pure), and 1 mg of polyvinylidene fluoride (PVDF, Thermo-Fisher Scientific, 99.9%) were mixed using a pestle and mortar for 2 min. Then, 1 drop of N-methyl-2-pyrrolidone (NMP, SRL, extra pure, 99.5%) was added to form a uniform slurry. This slurry was pipetted and pasted onto half of the conductive nickel foam (Nanoshel) using a doctor blade method. The electrode was then dried (90°C, 14 hr.) in a hot air oven.

All EC measurements (Potentiostat, EC-Lab® Express software, VSP-300) in dark and UV-vis light illumination (Hg-lamp, 250 W, 200–450 nm) conditions were carried out in an aqueous 0.5 M Na₂SO₄ (Merck; 99%) neutral electrolyte (pH = 7) using a 3-electrode setup configuration. Pt wire is used as a counter electrode, and Ag/AgCl (3.5 M KCl) is used as a reference electrode. The cyclic voltammetry (CV) or galvanostatic charge-discharge (GCD) tests were performed at various scan rates (5 to 100 mV/s) or current densities (0.5 to 5 A/g), respectively. The reported potential in this work is the reversible hydrogen electrode (V_{RHE}) potential, which is obtained using the equation: $V_{RHE} = V_{Ag/AgCl} + 0.205 + (0.059 \times \text{pH})$. For the half-cell supercapacitor, the specific capacitance (S ; F/g), energy density (E ; Wh/kg), and power density (P ; W/kg) were calculated using the equations: $S = (I \times t) / (\Delta V \times m)$; $E = 0.1388 \times S \times (\Delta V)^2$; and $P = (3600 \times D) / t$, where $I = 0.5$ A (applied current), t = discharge time (s), $m = 7$ mg (mass of the photoactive material), and $\Delta V = 0.8$ V (the applied potential window) [21].



Result and discussion

The XRD patterns and Raman spectra of as-synthesized pristine TiO₂ (S0) and various Cu-doped TiO₂ powder samples (1%-S1, 2%-S2, 3%-S3, and 4%-S4) are shown in **Figure 1**. The XRD peaks of all samples match well with a tetragonal crystal structure of an anatase TiO₂ phase (I4₁/amd space group, corner-sharing TiO₆ units, JCPDS data 073-1764). The average crystallite size and the lattice parameters of samples were estimated from the highest intensity 101 XRD peaks using a well-known Scherrer equation: $D = (0.9 \times \lambda) / [\beta \times \cos(\theta)]$, where $\lambda = 1.5406$ nm and β is the FWHM. The XRD pattern (**Figure 1a**) confirmed that incorporation of Cu into a tetragonal structure up to 3% enhances the crystallinity and enlarges the interplanar d -spacings (d_{101}), as well as affects the unit cell parameters (apical direction $\rightarrow c$ & equatorial direction $\rightarrow a$) (**Table 1**). This change in c/a ratio is attributed to the subtle balance between the size and oxidation states of the host Ti ions getting replaced by large-size foreign dopant Cu ions. [22-23]. Also, increasing doping amounts of Cu above 3% are expected to induce a disruption in the tetragonal symmetry of the unit cell as well as possibly leading to excessive defective oxygen states (vacancies), as inferred by the flipped unit cell parameters between S3 and S4 samples, i.e., their lattice parameters (a and c) and the corresponding interplanar d_{101} -spacings. (**Table 1**).

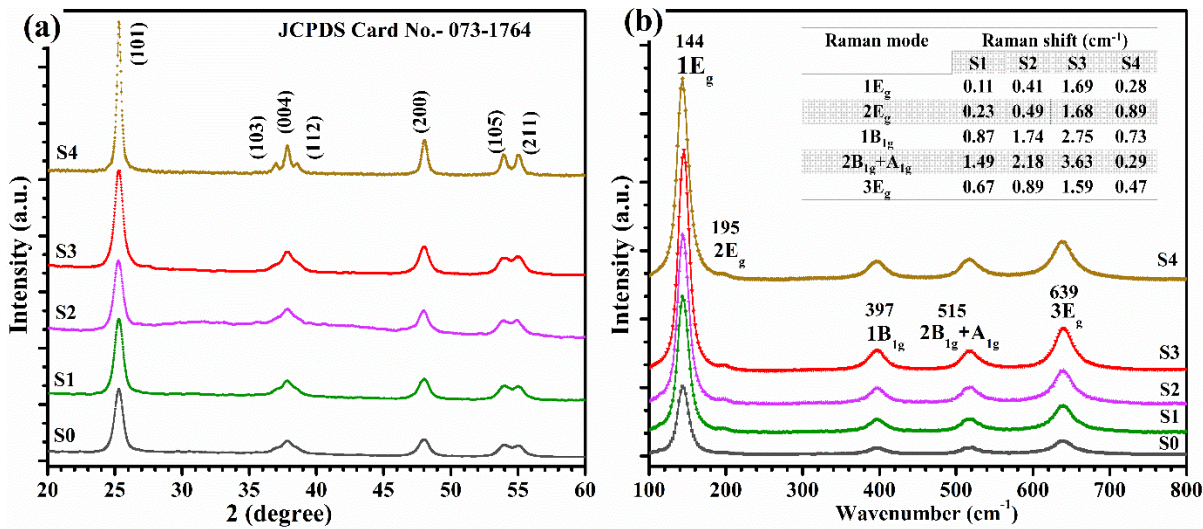
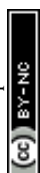


Figure 1. Indexed XRD pattern (a) and Raman spectra (b) of as synthesized powder samples. Pristine anatase TiO₂ (S0) and Cu-doped TiO₂ (1%-S1, 2%-S2, 3%-S3, 4%-S4). Insets in (b) are Raman shifts in S3 with respect to S0.

The effect of Cu doping amount on a host TiO₂ (TiO₆ octahedra) lattice becomes more visible in the vibrational Raman spectra (**Figure 1b**) of the samples. The active Eg Raman modes of the samples are symmetric stretching of Ti–O bonds, while the B1g and A1g are symmetric and antisymmetric bending motions of O–Ti–O, respectively. Raman-active modes for S0 are measured at 143 cm⁻¹ (E_{g1}), 193 cm⁻¹ (E_{g2}), 397 cm⁻¹ (1B_{1g}), 515 cm⁻¹ (2B_{1g}+A_{1g}), and 639 cm⁻¹ (E_{g3}) [24-25]. Up to 3% Cu doping, the increased intensity of the 1E_g vibration, along with the shifting of all Raman peaks, suggests that Cu doping enhances the coupling between Cu–O–Ti bonds and O–Ti–O bending modes. Thus, up to 3% Cu doping has a large effect on the apical bonds (*c*-axis) but only a minor effect on the equatorial bonds (*a*-axis), as indicated by a maximum wavenumber shift (inset, **Figure 1b**) for the S3 sample. However, the Raman peak shifting process reverses above 3% Cu doping, resulting in excessive distortion and perhaps the production of more structural defects in the unit cell [25-26]. Accordingly, both XRD and Raman studies showed that the S3 sample retains the crystal symmetry of its tetragonal lattice with optimum unit cell modifications (*c/a* = 2.44) and defective states. The extent of lattice modifications in Cu-doped TiO₂ samples is expected to alter their optical behavior and electronic characteristics. Note that modest crystal defects, like oxidation states of metallic cations and oxygen vacancies (electron donors), could act synergistically and might produce better electrical conductivity in a material, which is pivotal for its practical uses. Hence, the charge carrier pair separation efficiency in all the synthesized samples is studied using the PL emission spectroscopy technique.



190 The PL emission spectra plotted in **Figure 2a** indicated that the PL intensity
191 crossponding to chare carrier pair recombination does significantly vary with dopant (Cu)
192 amount. Doping with Cu impacted the PL emission intensity at 431 nm. The incorporation of
193 Cu ions into the Ti lattice site is expected to create the localized energy levels near the
194 bottom of conduction band (CB) edge. These localized states thus shall facilitate the non-
195 radiative recombination process, which would effectively suppress the defect-related
196 emissions [27]. This reduction in PL emission intensity at 431 nm thus can be attributed to
197 the distortion in the tetragonal TiO₂ lattice caused by Cu doping, which modifies the
198 electronic environment and reduces the pathways for the recombination of charge carrier
199 pairs [26-27]. In a Cu-doped TiO₂ sample, excessive Cu doping can detrimentally affect the
200 PL intensity. While Cu ions replacing Ti ions generate oxygen vacancies in the lattice, an
201 overabundance of such vacancies can also serve as self-trap centers for photoinduced charge
202 carrier pairs. This phenomenon is evident in the PL action spectra of the 4% Cu-doped TiO₂
203 (S4) sample. Consequently, the S3 sample exhibited the lowest PL emission intensity,
204 therefore indicating the highest conductivity among all synthesized samples [27]. Hence, this
205 PL emission analysis pointed out that among all the synthesized Cu-doped TiO₂ samples, the
206 lifetime of photogenerated charge carrier pairs is optimum for 3% Cu-doped TiO₂ (S3)
207 sample. As a result, at this point, we now examine the S3 sample and compare its
208 physicochemical characteristics with those of a reference (S0) sample.



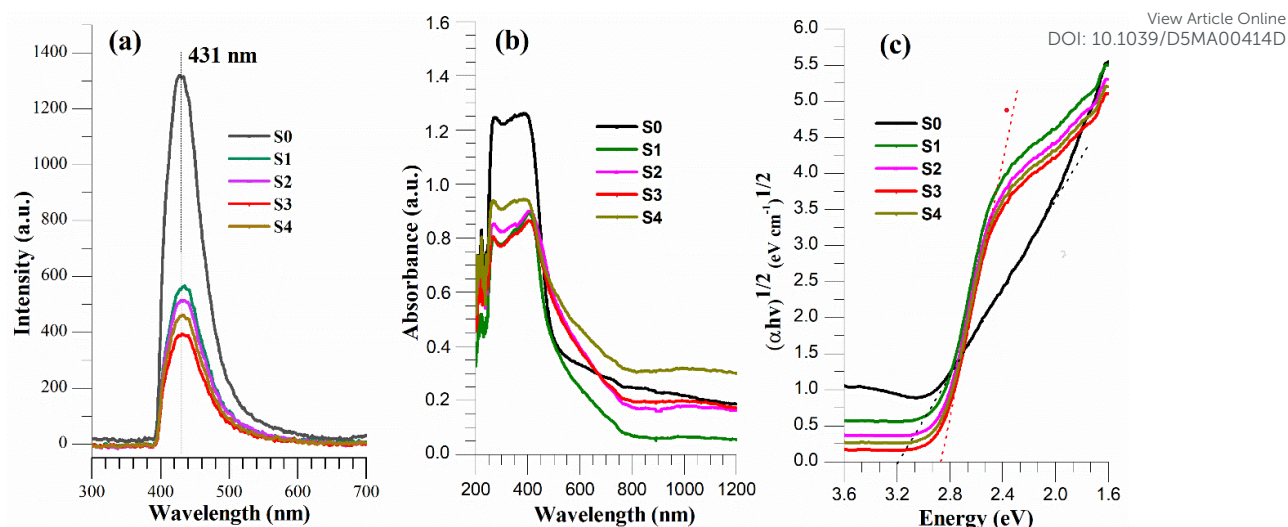


Figure 2. PL spectra (a) of all powders, highlighting S3 sample has the least recombination of charge charge-pairs. Optical absorption spectra (b) and Tauc $[(\alpha h\nu)^{1/2}$ vs. $h\nu$] plots (c) for samples.

Figure 2 (b-c) shows the UV-vis diffuse reflectance (DR) spectra and Tauc plots of all powder samples. The light absorption of pure anatase TiO_2 (S0) is attributed to the charge transfer from its valence band (VB; O_{2p} orbital) to the CB (Ti_{3d} , t_{2g} orbitals) [28-29]. Doping Cu into an anatase TiO_2 unit cell shifted the absorption edges towards the higher wavelength regime, which is expected to occur by a slight distortion of the cation-oxygen octahedra in the tetragonal lattice, i.e., Jahn-Teller distortion [26, 29]. Because Ti^{4+} has no response to visible light (above 400 nm) while Ti^{3+} does, so it is clear that the presence of Ti^{3+} ions and oxygen vacancies, as confirmed by XPS analysis later, contributed to a weaker (and stronger) absorbance in short (and long) wavelength ranges. The UV-vis DR spectra (**Figure 2b**) of S3 indicated that Cu doping into an anatase TiO_2 not only affects its VB (shallow/deep energy levels) but also influences the localized electronic charge in the CB. The Tauc plot analysis was used to estimate E_b values of all the samples. As expected, initially up to a 3% Cu doping quantity, E_b decreases (3.32 eV: S0, 2.92 eV: S1, 2.88 eV: S2, and 2.85 eV: S3) and then begins to rise (2.89 eV: S4) with further increasing the Cu doping amount above 3% (see

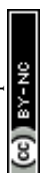


Table 1), and this result is fully supported by the PL analysis of samples. Moreover, ICP-MS analysis is used to determine the Cu content of the Cu-doped TiO₂ samples. This analysis confirmed that the Cu concentration within the TiO₂ lattice was 0.97% (S1), 0.97% (S1), 2.02% (S1), 2.98% (S2), and 4.03% (S4). These concentration values (at %) are fairly close to the Cu quantity used during their synthesis step. Thus, among all the Cu-doped TiO₂ samples, the smallest Eb around, 2.85 eV, is estimated for S3 sample only.

Open Access Article. Published on 31 July 2025. Downloaded on 8/4/2025 10:38:03 AM.
This article is licensed under a Creative Commons Attribution-NonCommercial 3.0 Unported Licence.

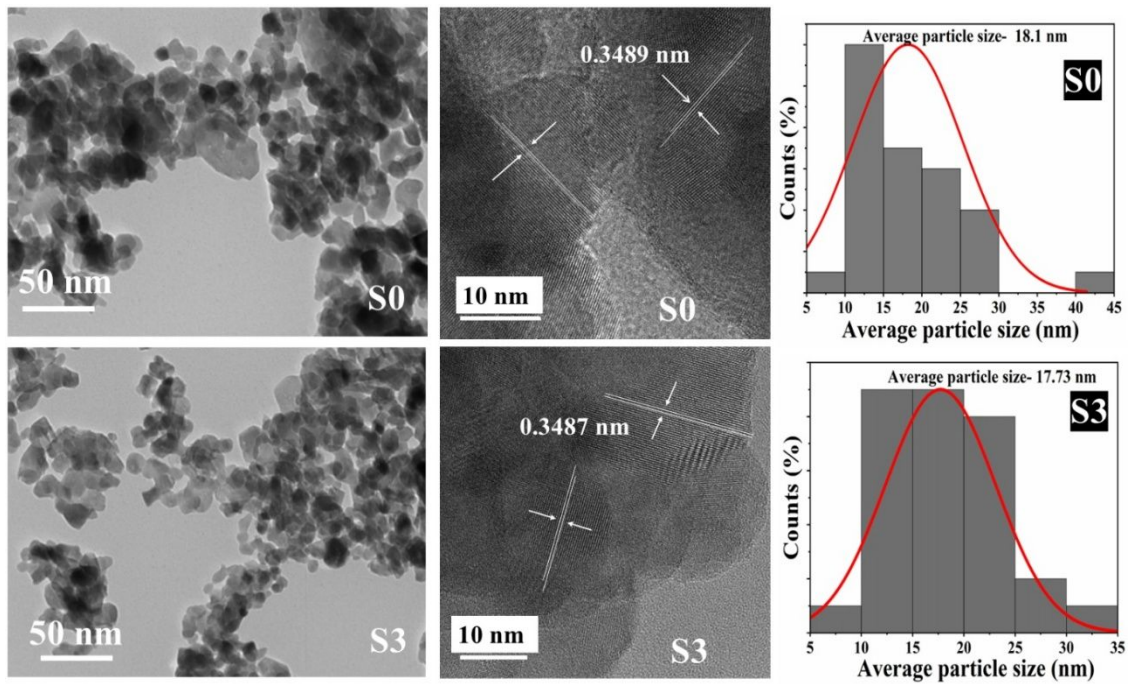
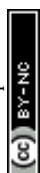



Figure 3. TEM images, HR-TEM images and particle size distribution histograms of S0 and S3 samples.

The microscopic TEM images, HR-TEM images, and particle size distribution of S3 and reference S0 samples are displayed in **Figure 3**. The TEM images of both samples showed uneven pebble-like morphologies of particles, and the average particle sizes estimated using TEM pictures range from 18.7 nm (S0) to 17.3 nm (S3), respectively. The well-ordered crystalline structure corresponding to an anatase type tetragonal TiO₂ crystal was further confirmed in the S0 and S3 samples by their respective HR-TEM images. There

is a good agreement found between the particle size and the interplanar d -spacing ($d_{(011)}$) estimated using XRD patterns and HR-TEM fringe spacing of the S0 and S3 samples (see **Table 1**). Thus, based on the thorough analysis carried out above using XRD, Raman spectroscopy, PL spectroscopy, UV-vis spectroscopy, and TEM microscopy, it is confirmed that S3 has the best electrically conductive properties and the lowest Eb of 2.85 eV compared to all the other samples (**Table 1**).

Generally, the recombination (**Figure 2a**) of charge carrier pairs in a material takes place via the existence of its defective anionic states (oxygen vacancies). Hence, the XPS characterization technique is used to identify the chemical states of metallic and the oxygen species in S0 and S3 samples. **Figure 4 (a-d)** illustrates the high-resolution XPS spectra of Ti, Cu, and oxygen species in S0 and S3 samples. Using the peak fitting (function: pseudo-Voigt function, Lorentzian to Gaussian distribution, set ratio~ 0.1), the binding energy (BE) values analysis of Ti and Cu peaks indicated the coexistence of Ti^{4+} (Ti^{3+}) and Cu^{2+} (Cu^{1+}) oxidation states in the respective S0 and S3 samples [30-31]. Note that in S0 itself, the existence of Ti^{3+} is suspected to be caused by the reducing nature of the solvent (2-methoxyethanol) used during its synthesis, which could reduce Ti ions from the Ti^{4+} to the Ti^{3+} state (see **Figure 4b**). The lower BE (ca. 0.1 eV) values of the Ti doublet ($2p_{3/2}$ and $2p_{1/2}$) thus confirm the formation of Ti-O-Cu bonds in the S3 sample (**Figure 4a**). This BE shift likely originated due to an electron density transfer from less electronegative metallic Ti^{4+} (Ti^{3+}) ions to the more electronegative metallic Cu^{2+} (Cu^{1+}) ions [32-33]. **Figure 4b** shows the high-resolution XPS spectra of Cu species in S3 sample. The fitted Gaussian peaks in XPS spectra were located at BE values of 931.9 eV and 933.1 eV, respectively, which represent the bivalent Cu^{1+} and Cu^{2+} states. The Ti^{3+} and Cu^{1+} defects might have arisen to compensate for the oxygen vacancies in the lattice, and a reasonable Ti^{3+} to Ti^{4+} ratio often could lead to an improved light absorption due to the formation of intermediate energy levels



just below its CB edge caused by the localized Ti^{3+} species and lattice oxygen (O_v) vacancies [37]. This significant reduction in the Eb (see **Table 1**) from 3.32 eV (S0) to 2.85 eV (S3) is clearly observed in the Tauc plot result of the samples (see **Figure 2c**).

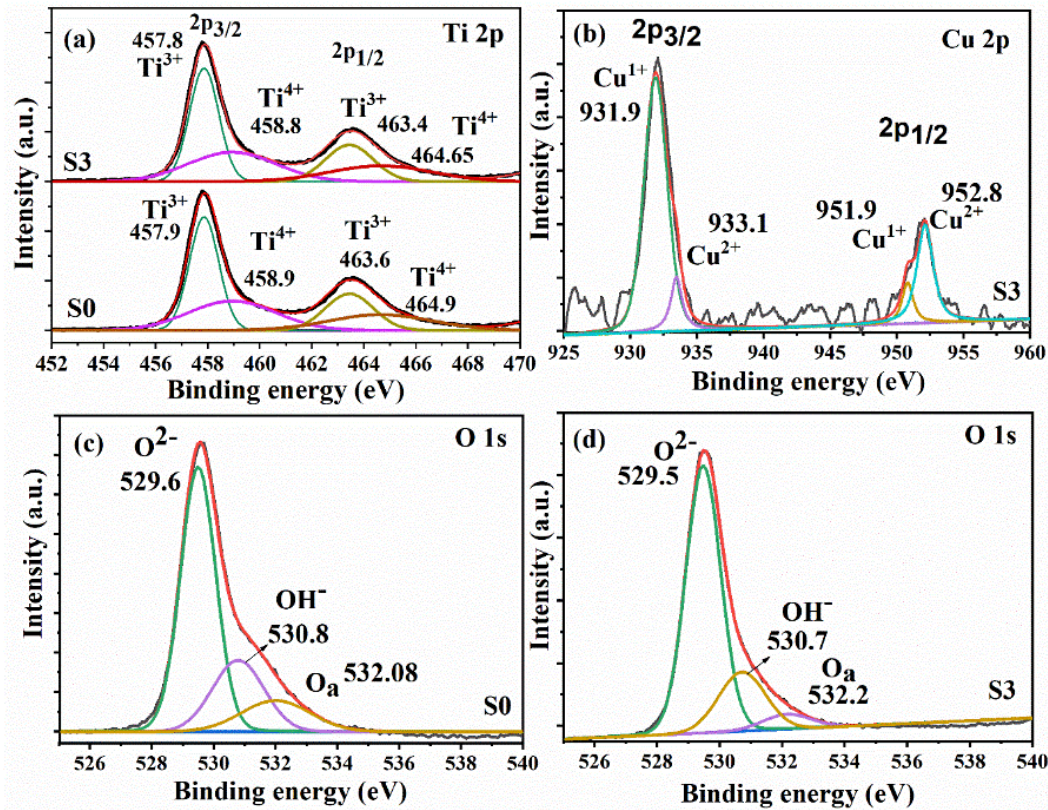


Figure 4. High-resolution XPS spectra of Ti, Cu, and O (lattice oxygen $\rightarrow \text{O}^{2-}$; surface hydroxy radicals $\rightarrow \text{OH}^-$; surface adsorbed oxygen $\rightarrow \text{O}_\text{a}$) of S0 and S3 samples. BE~284.6 eV of surface advantages C1s peak is used a calibrating reference.

Figure 4 (c-d) displays the O1s high-resolution XPS spectra of the S0 and S3 samples with the existence of all three types of oxygen species [30, 34]. Deconvolution analysis (Gaussian peak fitting) of the O1s peak is used to determine the lattice oxygen (O^{2-}) concentration, and a little 5% reduction in its value from 0.362 (S0) to 0.312 (S3) suggests that the S3 sample has a greater O_v i.e., electrons donors, than the S0 sample [35]. This is in line with the results of PL spectroscopy (**Figure 2a**) and CB and VB analysis carried out using UV-vis spectroscopy (**Figure 2b**). Additionally, the EPR spectra shown in **Figure 5**

confirmed that the S3 sample has more O_V and defect states than the S0 sample at room temperature condition. Due to the low concentration of intrinsic O_V and Ti^{3+} centers, the S0 sample exhibited a very weak EPR signal at $g \approx 2.0 - 2.07$ (near around 3400 Gauss). The S3 sample, on the other hand, displayed a noticeably stronger and wider EPR signal centered at $g \approx 2.07$, suggesting a large increase in native paramagnetic (O_V) sites. This enhancement is likely due to the substitution of Ti^{4+} ions by Cu^{2+} ions, which leads to charge compensation through the formation of O_V and Ti^{3+} (Cu^{1+}) centers. The broadening of the EPR signal further suggests possible interactions between the Cu^{2+} ions and the anatase TiO_2 lattice [36]. These EPR results provide strong bulk-sensitive evidence for defect generation, complementing the surface-sensitive XPS findings and confirming that Cu doping effectively introduces oxygen vacancies in the anatase TiO_2 crystal structure.

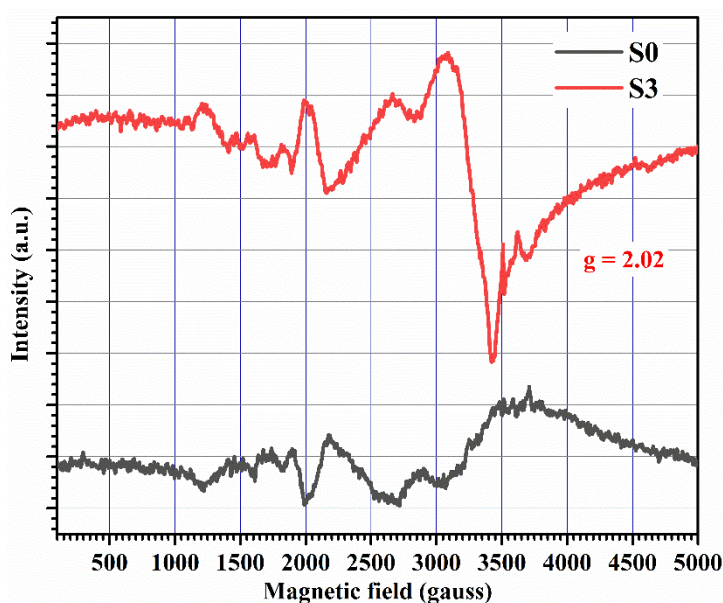


Figure 5. X-band frequency (9.843 GHz) EPR spectra of S0 and S3 samples at room temperature.

Thus, through the physicochemical and optoelectronic characterization studies employing XRD, Raman, PL, UV-vis, XPS, and EPR techniques, it was concluded that the



smaller optical bandgap in the S3 sample is caused by a modest and optimum lattice distortion ($c/a = 2.442$) caused by Ti^{3+} , Cu^{1+} , and O_V sites, which in turn leads to the higher electrical conductivity of intrinsic charge carrier pairs [33]. Here onwards, we solely focus on assessing the photo-driven catalytic and electrocatalytic redox abilities of the S3 sample and compare them to the reference S0 sample. The EC activities of S0 and S3 electrodes were evaluated using CV and GCD techniques under dark as well as UV-vis light (Hg-lamp, 250 W, 200–450 nm) irradiation conditions.

Table 1. Physicochemical, photo-catalytic and electro-catalytic properties of samples: Crystallite size (D), optical bandgap (E_b), lattice oxygen species amount (O^{2-}), electrocatalytic capacitance in UV-vis light (250 W Hg-lamp; S_L) and dark (S_D) conditions, energy density in light (E_L) and dark (E_D) conditions, power density in light (P_L) and dark (E_D) conditions, photo-degraded concentration (C_RB) and 1st order rate-constant (k_1) for RhB dye (25 ppm). Pristine anatase TiO_2 (S0) and various Cu-doped anatase TiO_2 (1%-S1; 2%-S2, 3%-S3, 4%-S4).

Sample	D^\dagger	a	c/a	d_{101}^\dagger	E_b	O^{2-}	S_D^\square	E_D	P_D	C_RB	k_1
		c					S_L^\square	E_L	P_L		
	(nm)	(Å)		(nm)	(eV)	(%)	(F g^{-1})	(Wh kg^{-1})	(W kg^{-1})	(%)	($\mu\text{ s}^{-1}$)
S0	15.3	3.752	2.526	0.3485	3.32	0.362	188.5	16.76	252.9	42.5	6
	[18.1]	9.48		[0.3489]			247.1	21.96	198.6		
S1	14.9	3.753	2.488	0.3482	2.92						
		9.34									
S2	14.8	3.754	2.469	0.3483	2.88						
		9.27									
S3	14.3	3.768	2.442	0.3486	2.85	0.312	295.6	26.28	209.9	95.03	36
	[17.3]	9.203		[0.3487]			346.3	30.78	194.7		
S4	15.1	3.734	2.520	0.3471	2.89						
		9.41									

[†] Inside parentheses using TEM (histograms) and HR-TEM analysis.

[□] Using GCD curves (at 0.5 A/g applied current density).

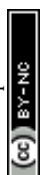
Figure 6 shows the comparison of current density vs. applied potential (vs. V_RHE)

characteristics curves of S0 and S3 electrodes with fixed scan rates under dark and UV-vis



light (Hg-lamp, 250 W) illumination conditions. These CV curves measured in an aqueous 0.5 M Na₂SO₄ electrolyte reveal a pseudocapacitive-type redox behavior of both the S0 or S3 electrodes, respectively [37]. A straightforward indicator of the specific capacity is the loop area of CV curves. The capacitive performance of either electrode increases with an increase in scan rate. As expected, the significantly improved capacitive capabilities of the Cu-doped TiO₂ (S3) electrode than to a reference TiO₂ (S0) electrode are demonstrated by its larger loop areas at any set scan rate, irrespective of both dark and UV-vis light irradiation conditions. **Figure 7** displays the GCD, i.e., the charging/discharging vs. time curve of the electrodes. Irrespective of light conditions, the electrodes generate a potential window of around 0.8 V (vs. V_{RHE}) across various applied current densities (5–0.5 A/g). A decrease in discharging current density from 5 to 0.5 A/g under dark conditions led to increased discharging time under light conditions, indicating enhanced supercapacitive behavior. A nearly triangular shape with a slight deviation of the GCD curves, indicating the pseudocapacitive behavior of the electrodes, correlated with the CV results [20, 37].

Under dark conditions and at a fixed low scan rate of 5 mV/s, the calculated specific capacitance of S0 and S3 was approximately 188 F/g and 295 F/g, respectively. Under dark conditions, the nearly 57% improved electrocatalytic redox performance of S3 over S0 can be directly ascribed to a superior charge carrier conductivity caused by a moderate Cu doping amount [20] (see **Figure 2a**). Under 250 W of UV-vis light intensity, the specific capacitance of S0 and S3 improved to nearly 30% (247 F/g) and 40% (346 F/g), which is attributed to extra charge carriers generated by light irradiation (see **Figure 2c**). The S value of Cu-doped TiO₂ (S3; 346.3 F/g) under light conditions was 84% higher than the S value of TiO₂ (S0; 188.5 F/g) under dark conditions. The energy density (E) and power density (P) values for the S0 and S3 electrodes are listed in **Table 1**. The S3 electrode demonstrated about a 57% greater E value and a 17% lower P value than the S0 electrode under dark conditions.



Nevertheless, the S3 sample displayed almost the same P value and around 40% greater E_{redox} value than the S0 sample when exposed to 250 W UV-vis light. This photoinduced charge generation mechanism complements conventional charge storage methods, such as pseudocapacitance, activated during the electrical charging-discharging.

The long-term photoelectrochemical cyclic stability of the S3 electrode during the GCD test is displayed in **Figure 7e**. At an applied current density of 5.0 A/g, it retained 94.4% of its initial capacitance after 10000 cycles.

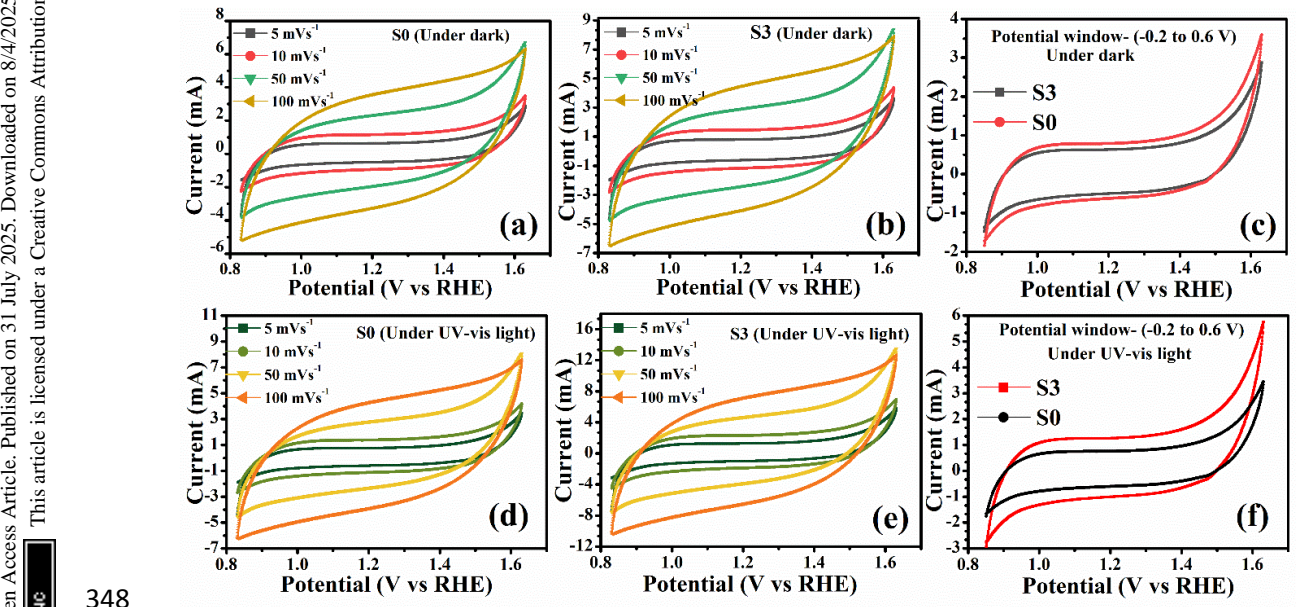


Figure 6. Scan rate CV curves of S0 and S3 electrodes (active material~ 1 mg, area~0.5 cm²) under dark and UV-vis light irradiation (250 W Hg-lamp) in a 0.5 M aqueous Na₂SO₄ electrolyte. Applied scan rate is 5 mV s⁻¹ (Figure 6c and 6f).

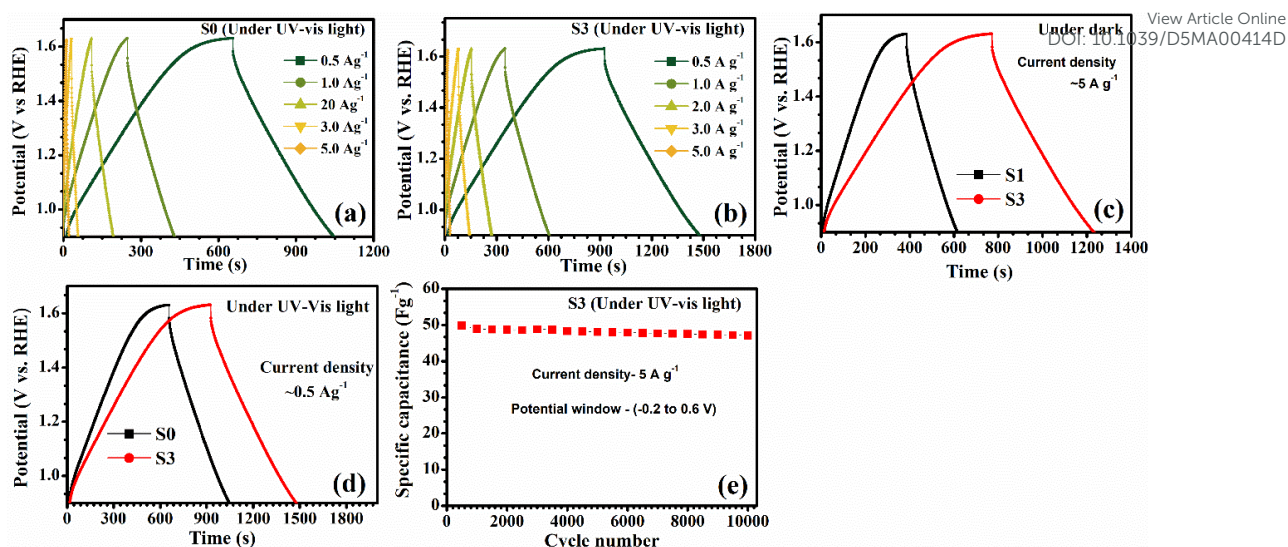


Figure 7. GCD curves (a-d) at various applied current densities and the photoelectrochemical stability (e) of S0 and S3 electrodes under dark and UV-vis light irradiation conditions (see Figure 6). Applied current density is 0.5 A g⁻¹ (Figure 7c and 7d).

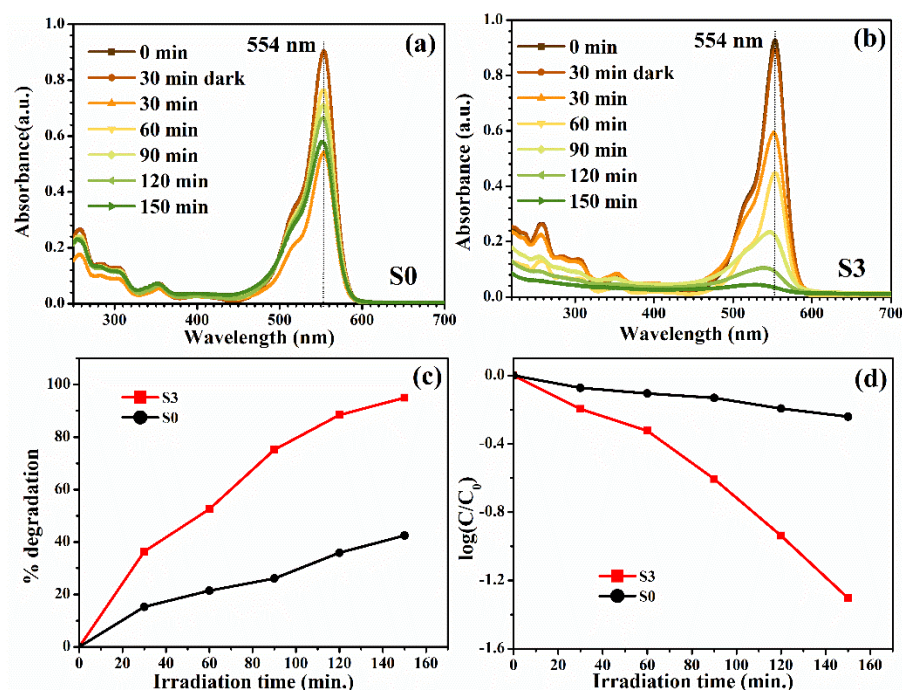


Figure 8. Time-course dependent absorption spectra of RhB dye (25 ppm) dissociation using S0 and S3 sample as photocatalytic material. The light source is a 250 W Hg-lamp (200–450 nm).

Figure 8 illustrates the time-dependent photocatalytic dissociation of RhB dye (absorbance maximum at 554 nm) using 100 mg of photocatalyst sample. RhB is a common hazardous and carcinogenic contaminant found in industrial wastewater. Therefore, it is frequently used as a probe molecule to assess the photocatalytic efficiency. It should be noted that the S0 (S3) sample eliminated 1.7% (3.2%) of a 25 ppm RhB dye concentration under dark ambient conditions through the adsorption process in 30 minutes and thereafter (tested up to 4 hours). However, these S0 and S3 samples, which have nearly identical nanoparticle shapes and sizes (**Figure 3**), exhibited approximately 42.5% and 95.03% photodissociation of RhB concentrations after 150 minutes of continuous light illumination. This over two-fold enhancement in the photocatalytic degradation efficiency of S3 is directly attributed to its lower E_b (2.85 eV) compared to S0 (3.32 eV), indicating a higher concentration of intrinsic charge pairs and their effective separation, as previously demonstrated by the optoelectronic analysis using UV-vis and PL emission studies (**Figures 2**). The linear (least squares) fit plot of $\log(C/C_0)$ against the elapsed photocatalytic reaction time provided the first-order reaction rate constant for samples. A nearly 6-fold increase in photocatalytic reaction rate is demonstrated by the S3 sample than to the S0 sample (**Table 1**) [20]. Note that a modest doping concentration of Cu in TiO_2 introduces defect (Ti^{3+} and oxygen vacancies) levels that help in reducing the band gap and promoting the separation of photoinduced electron-hole pairs. Specifically, the Cu^{2+} ions, possessing a lower valence than Ti^{4+} , introduce stable oxygen vacancies mostly located at the O site next to the $\text{Cu}^{1+}/\text{Cu}^{2+}$ dopants in the lattice [38]. These oxygen vacancies and Cu^{1+} act as active sites for molecular dissociation and facilitate hole capture, thereby reducing electron-hole recombination. However, excessive Cu doping in anatase TiO_2 can negatively impact its catalytic performance, as indicated by the PL results (**Figure 2a**). The elevated concentrations of Cu above 3% not only destroy the symmetry of the tetragonal lattice (**Figure 1, Table 1**), but also its Cu^{2+} state easily traps the



photogenerated electrons, leading to the formation of extra Cu^{1+} or Ti^{3+} ions. This scenario could result in a short-circuiting effect where both photogenerated charge carriers (electrons and holes) are rapidly consumed (recombination) [39].

Conclusions

The global need for energy solutions and environmental pollution have increased dramatically, so in this regard, electrochemical supercapacitors and photocatalysis have become promising technologies to provide rapid power delivery and energy sustainability in a variety of practical applications. In this work, we synthesized Cu-doped anatase TiO_2 powders using a simple alcohothermal technique. When Cu is incorporated into anatase TiO_2 , a considerable lattice distortion is produced, and a moderate to severe distortion can either improve or deteriorate the optoelectronic characteristics and vice versa. Interestingly, a significant increase in the photocatalytic efficiency of more than two times and an 84% enhancement in electrocatalytic supercapacitance under UV-vis light conditions is achieved with an ideal 3% Cu doping concentration. This remarkable boost in catalytic performance is directly attributed to improved light absorption and an efficient separation of charge carrier pairs. This work highlights the possibility of further increasing the catalytic efficiencies of Cu-doped anatase TiO_2 through lattice optimizations, opening the door for creating sophisticated photocatalyst and electrocatalyst materials with exceptional functional qualities for energy and environmental applications.

Conflict of Interest

There is no conflict of interest to declare.

References



- 407 [1] Fathima, H. *Problems in Conventional Energy Sources and Subsequent Shift to Green* View Article Online
DOI: 10.1039/D5MA00414D
408 *Energy*. International Conference on Engineering Technology and Science-(ICETS'14),
409 Rasipuram. (February 2014) Vol. 3, Special Issue 1.
- 410 [2] Kartal, M. T. *Renewable Energy* 184 (2022) 871-880.
411 doi:<https://doi.org/10.1016/j.renene.2021.12.022>
- 412 [3] Jaiswal, K. K., Chowdhury, C. R., Yadav, D., Verma, R., Dutta, S., Jaiswal, K. S.,
413 Karuppasamy, K. S. K. *Energy Nexus* 7 (2022) 100118.
414 doi:<https://doi.org/10.1016/j.nexus.2022.100118>
- 415 [4] Shakthivel, D., Dahiya, A. S., Mukherjee, R., & Dahiya, R. *Current Opinion in Chemical*
416 *Engineering* 34 (2021) 100753 doi:<https://doi.org/10.1016/j.coche.2021.100753>
- 417 [5] Ahn, J., Lee, S. H., Song, I., Chidchob, P., Kwon, Y., & Oh, J. H.. *Device* 1(5) (2023)
418 100176 doi:<https://doi.org/10.1016/j.device.2023.100176>
- 419 [6] Rafique, M., Hajra, S., Irshad, M., Usman, M., Imran, M., Assiri, M. A., & Ashraf, W. M.
420 *ACS Omega* 8(29) (2023) 25640-25648 doi:10.1021/acsomega.3c00963
- 421 [7] Khan, H., & Shah, M. U. H. *Journal of Environmental Chemical Engineering*, 11(6)
422 (2023) 111532.
- 423 [8] Dell'Edera, M., Lo Porto, C., De Pasquale, I., Petronella, F., Curri, M. L., Agostiano, A.,
424 & Comparelli, R. *Catalysis Today* 380 (2021) 62-83.
425 doi:<https://doi.org/10.1016/j.cattod.2021.04.023>
- 426 [9] Nunes Simonetti, E. A., Cardoso de Oliveira, T., Enrico do Carmo Machado, Á.,
427 Coutinho Silva, A. A., Silva dos Santos, A., & de Simone Cividanes, L. *Ceramics*
428 *International* 47(13) (2021) 17844-17876.
429 doi:<https://doi.org/10.1016/j.ceramint.2021.03.189>
- 430 [10] Tian, X., Cui, X., Lai, T., Ren, J., Yang, Z., Xiao, M., Wang, Y. *Nano Materials*
431 *Science* 3(4) (2021) 390-403 doi:<https://doi.org/10.1016/j.nanoms.2021.05.011>
- 432 [11] Khan, H., & Shah, M. U. H. *Journal of Environmental Chemical Engineering*, 11(6)
433 (2023) 111532. doi:<https://doi.org/10.1016/j.jece.2023.111532>
- 434 [12] Parmar, K. P. S., Ramasamy, E., Lee, J., & Lee, J. S. *Chemical Communications*,
435 47(30) (2011) 8572-8574 doi:10.1039/C1CC12150B
- 436 [13] Parmar, K. P. S., Ramasamy, E., Lee, J. W., & Lee, J. S. *Scripta Materialia*, 62(5)
437 (2010) 223-226 doi: <https://doi.org/10.1016/j.scriptamat.2009.11.001>
- 438 [14] Mogal, S. I., Mishra, M., Gandhi, V. G., & Tayade, R. J. *Materials Science Forum*
439 734 (2013) 364-378 doi:10.4028/www.scientific.net/MSF.734.364



- 440 [15] Shi, N., Liu, G., Xi, B., An, X., Sun, C., Liu, X., & Xiong, S. *Nano Research* 16(7) New Article Online
DOI: 10.1039/D5MA00414D
441 (2023) 9398-9406 doi:10.1007/s12274-023-5604-3
- 442 [16] Sangeetha, M., Kalpana, S., Senthilkumar, N., & Senthil, T. S *Optik* 301 (2024)
443 171687 doi:<https://doi.org/10.1016/j.ijleo.2024.171687>
- 444 [17] Jha, B., Chaule, S., & Jang, J.-H. *Materials Chemistry Frontiers*, 8,(2024).
445 doi:10.1039/D3QM01100C
- 446 [18] Chen, B., Meng, Y., Sha, J., Zhong, C., Hu, W., & Zhao, N. *Nanoscale*, 10(1) (2018)
447 34-68, 2018, doi:10.1039/C7NR07366F
- 448 [19] Li, Z., Wang, X., Wang, X., Xiao, T., Zhang, L., Lv, P., & Zhao, J. *International*
449 *Journal of Hydrogen Energy* 43(18) (2018) 8859-8867
450 doi:<https://doi.org/10.1016/j.ijhydene.2018.03.138>
- 451 [20] Chaudhary, S., Parmar, K. P. S., Brajpuriya, R., Rawat, B. S., & Vij, A. *Energy*
452 *Technology* 13(3) (2025) 2401138 doi: <https://doi.org/10.1002/ente.202401138>
- 453 [21] Maher, M., Hassan, S., Shoueir, K., Yousif, B., & Abo-Elsoud, M. E. A. *Journal of*
454 *Materials Research and Technology* 11 (2021) 1232-1244.
- 455 [22] Rahm, M., Hoffmann, R., & Ashcroft, N. Atomic and Ionic Radii of Elements 1–96.
456 *Chemistry - A European Journal* 22 (2016) doi:10.1002/chem.201602949
- 457 [23] Maier, R. A., Johnston-Peck, A. C., & Donohue, M. P. *Advanced Functional*
458 *Materials* 26(45) (2016) 8325-8333 doi: <https://doi.org/10.1002/adfm.201602156>
- 459 [24] Ohsaka, T., Izumi, F., & Fujiki, Y. *Journal of Raman Spectroscopy* 7(6) (1978) 321-
460 324 doi:<https://doi.org/10.1002/jrs.1250070606>
- 461 [25] Taudul, B., Tielens, F., & Calatayud, M. *Nanomaterial(Basel)*. 13(12) (2023) 1856.
- 462 [26] Halcrow, M. A. *Chemical Society Reviews* 42(4) (2013) 1784-1795.
463 doi:10.1039/C2CS35253B
- 464 [27] Liqiang, J., Yichun, Q., Baiqi, W., Shudan, L., Baojiang, J., Libin, Y., Jiazhong, S.
465 *Solar Energy Materials and Solar Cells* 90(12) (2006) 1773-1787.
466 doi:<https://doi.org/10.1016/j.solmat.2005.11.007>
- 467 [28] Braginsky, L., & Shklover, V. *The European Physical Journal D* 9 (1999) 627-630
468 doi:10.1007/s100530050514
- 469 [29] Choudhury, B., Dey, M., & Choudhury, A. *International Nano Letters* 3 (2013).
470 doi:10.1186/2228-5326-3-25



- [30] Pourhakkak, P., Taghizadeh, A., Taghizadeh, M., Ghaedi, M., & Haghdoust, S. Chapter 1 - Fundamentals of adsorption technology. In M. Ghaedi (Ed.), *Interface Science and Technology* (Vol. 33, pp. 1-70): Elsevier, 2021 .
- [31] Greczynski, G., & Hultman, L. *Progress in Materials Science* 107 (2020) 100591. doi:<https://doi.org/10.1016/j.pmatsci.2019.100591>
- [32] Ivanova, T. M., Maslakov, K. I., Sidorov, A. A., Kiskin, M. A., Linko, R. V., Savilov, S. V., Eremenko, I. L. *Journal of Electron Spectroscopy and Related Phenomena* 238 (2020) 146878 doi:<https://doi.org/10.1016/j.elspec.2019.06.010>
- [33] Tantardini, C., & Oganov, A. R. *Nat Commun* 12(1) (2021) 2087 doi:10.1038/s41467-021-22429-0
- [34] Idriss, H. J. S. S. *Surface Science*. 712 (2021) 121894.
- [35] Rabchinskii, M. K., Shnitov, V. V., Brzhezinskaya, M., Baidakova, M. V., Stolyarova, D. Y., Ryzhkov, S. A., Brunkov, P. N. *Nanomaterials (Basel)* 13(1) (2022). doi:10.3390/nano13010023
- [36] Misra, S. K., Andronenko, S. I., Tipikin, D., Freed, J. H., Somani, V., Prakash, O. *Journal of Magnetism and Magnetic Materials*, 401 (2016) 495-505 <https://doi.org/10.1016/j.jmmm.2015.10.072>
- [37] Pascariu, P., Homocianu, M., Vacareanu, L., & Asandulesa, M. (*Polymers* 14(21) (2022) doi:10.3390/polym14214739
- [38] Navas, J., Sánchez-Coronilla, A., Aguilar, T., Hernández, N. C., Desirée, M., Sánchez-Márquez, J., Zorrilla, D., Fernández-Lorenzo, C., Alcántara, R., Martín-Calleja, J. Experimental and theoretical study of the electronic properties of Cu-doped anatase TiO₂. *Phys. Chem. Chem. Phys.* 16 (8) (2014) 3835-3845. <https://doi.org/10.1039/C3CP54273D>
- [39] Snehamol M., Priyanka G., Stephen R., Vignesh K., Ciara B., Steven J. H., John B., Michael N., Suresh C. P. *Appl. Sci.* 8(11) (2018) 2067. <https://doi.org/10.3390/app8112067>



Data Availability Statement

[View Article Online](#)
DOI: 10.1039/D5MA00414D

On request, all the data can be obtained freely via email correspondence with the author.

